

Preparation of g-C₃N₄/MoS₂ Composite Material and Its Visible Light Catalytic Performance

Yu Fan

Yan'an University

Yan-ning Yang (✉ yangyanning@yau.edu.cn)

Yan'an University <https://orcid.org/0000-0002-0519-3484>

Chen Ding

Yan'an University

Research Article

Keywords: g-C₃N₄ nanosheet, MoS₂ nanosheet, g-C₃N₄/MoS₂, ultrasonic composite method, visible light photocatalysis

Posted Date: June 18th, 2021

DOI: <https://doi.org/10.21203/rs.3.rs-627855/v1>

License: © ⓘ This work is licensed under a Creative Commons Attribution 4.0 International License.

[Read Full License](#)

Version of Record: A version of this preprint was published at Journal of Inorganic and Organometallic Polymers and Materials on September 17th, 2021. See the published version at <https://doi.org/10.1007/s10904-021-02099-7>.

Abstract

The g-C₃N₄ nanosheet was prepared by calcination method, the MoS₂ nanosheet was prepared by hydrothermal method. The g-C₃N₄/MoS₂ composites were prepared by ultrasonic composite in anhydrous ethanol. X-ray diffraction (XRD), scanning electron microscopy (SEM), transmission electron microscopy (TEM), X-ray photoelectron spectroscopy (XPS), ultraviolet-visible spectroscopy (UV-Vis), and photoluminescence (PL) techniques were used to characterize the materials. The photocatalytic degradation of Rhodamine B (Rh B) by g-C₃N₄/MoS₂ composites with different mass ratios was investigated under visible light. The results show that a small amount of MoS₂ combined with g-C₃N₄ can significantly improve photocatalytic activity. The g-C₃N₄/MoS₂ composite with a mass ratio of 1:8 has the highest photocatalytic activity, and the degradation rate of Rh B increases from 50% to 99.6%. The main reason is that MoS₂ and g-C₃N₄ have a matching band structure. The separation rate of photogenerated electron-hole pairs is enhanced. So the g-C₃N₄/MoS₂ composite can improve the photocatalytic activity. The photocatalytic mechanism was proposed through the active matter capture experiment.

1 Introduction

Printing and dyeing wastewater, as a kind of industrial wastewater, has a large discharge. According to statistics, every year the textile field of sewage discharge up to more than 900 million tons, sewage emissions accounted for the entire industrial wastewater discharge number 6. Among them, the main component of textile industry wastewater is printing and dyeing wastewater. Therefore, the treatment of printing and dyeing wastewater mainly affects the treatment effect of textile wastewater. Printing and dyeing wastewater has many components, often containing slurry, auxiliaries and fuels, high chroma, toxic and harmful, difficult to dispose. Direct discharge without treatment or improper treatment will seriously damage the ecological environment, threaten human health [1]. Traditional wastewater treatment methods include physical methods, advanced oxidation methods and biological methods. Photocatalytic technology can effectively decompose pollutants, is a green environmental protection treatment technology. It has the advantages of low energy consumption, easy operation, mild reaction conditions and no secondary pollution [2]. Photocatalysis has attracted the attention of many researchers around the world since 1972 when the study of photocatalytic decomposition of water under ultraviolet light was reported on a single crystal TiO₂ electrode [3]. Wide-band gap semiconductor materials such as TiO₂ and ZnO have been extensively studied. But they react only in violet light and are not very efficient, which also hampers their use [4]. After decades of exploration and development, a large number of new semiconductor photocatalysts have been developed, such as metal oxide [5–7], metal sulfide [8, 9], silver halide [10, 11], silver phosphate [12, 13], layered bismuth oxyhalide [14, 15], and so on. New semiconductor photocatalysts can form a suitable bandwidth and use sunlight more efficiently.

In 2009, the team of Wang Xinchun [16] reported a kind of graphite-structured layered material for the first time, which was named graphite phase carbon nitride (g-C₃N₄). It has a band gap of 2.7 eV. It shows a

very strong ability of oxidation and photocatalytic decomposition of organic matter under visible light irradiation, which has been widely paid attention to by researchers [17]. However, the g-C₃N₄ has some shortcomings that make its photocatalytic effect poor. For example, its specific surface area is relatively small, and the photo-generated electron-holes are easy to recombine. These shortcomings make it unable to stand alone in the field of photocatalysis. For this reason, researchers have tried many methods to improve the photocatalytic activity of g-C₃N₄. Such as element doping [18, 19], precious metal deposition [20, 21], and semiconductor compounding [22, 23]. At present, two-dimensional (2D) materials can be used in many places, including the field of photocatalysis by their super large specific surface area and suitable forbidden band width. It is one of the frontiers of research. The 2D MoS₂ has attracted much attention due to its excellent properties, good electrical conductivity, and narrow band gap. In addition, because it has a unique energy band structure and good lattice matching, MoS₂ matches well with g-C₃N₄, which can effectively accelerate the transfer of electrons and holes [24]. Yan et al. [25] used the ball milling method to compound g-C₃N₄ with MoS₂ to disintegrate pollutants under visible light irradiation, which significantly improved the photocatalytic activity of semiconductor materials. Experimental facts have proved that the combination of g-C₃N₄ and MoS₂ can effectively promote the separation rate of photogenerated electron-hole pairs and improve the photocatalytic activity of g-C₃N₄. Ge et al. [26] loaded MoS₂ on the surface of g-C₃N₄ by the impregnation-calcination method, of which 0.5% (w/w) MoS₂/g-C₃N₄ photocatalytic hydrogen production activity was the best, which was about 11.3 times that of single g-C₃N₄. Li et al. [27] used the chemical ultrasonic method to prepare g-C₃N₄/MoS₂ composite catalyst successfully. The results showed that the addition of MoS₂ significantly improved the catalytic activity of g-C₃N₄ on Rh B and methylene blue under visible light. A large number of experiments show that MoS₂ is a good promoter.

In this paper, the g-C₃N₄/MoS₂ composite was prepared by a simple ultrasonic composite method. Its photocatalytic performance was verified by the degradation rate of Rh B under visible light irradiation. The crystal structure, microstructure and luminescence properties of the samples were characterized and analyzed by XRD, SEM, TEM, XPS, UV-Vis, and PL. The mechanism of photocatalytic degradation was further discussed by capturing active substances.

2 Experiment

2.1 Preparation of photocatalysts

Melamine, Rh B and ethanol were purchased from Sinopharm Chemical Reagent Co., Ltd (China). All reagents were at the analytical level. They were used without any further purification.

The g-C₃N₄ powder was prepared by thermal polymerization with melamine as raw material. 10 g of melamine powder was heated to 550°C in a muffle furnace at the rate of 5 °C/min for 5 h. At the end of the reaction, the g-C₃N₄ powder was obtained by grinding.

MoS₂ nanosheets were prepared by the one-step hydrothermal method. Firstly, 0.28 mmol ammonium molybdate and 10 mmol thiourea were dissolved in 10 mL of deionized water. After magnetic stirring for 30 min, the solution was fully dissolved into a uniform solution by ultrasound for 30 min. Secondly, poured the solution into a 50 mL high-pressure reactor. After sealing, the reaction kettle was placed in the electric heating blast drying oven for hydrothermal reaction. The temperature was set at 200 °C, and the time was set at 10 h. Thirdly, the precipitate was cleaned repeatedly with deionized water and anhydrous ethanol. Finally, the precipitate was dried in a 60 °C oven for 10 h to collect black MoS₂ powder.

The g-C₃N₄/MoS₂ composites were obtained by simple ultrasonic composite. Firstly, 0.2 g g-C₃N₄ powder and 0.025 g MoS₂ powder were weighed and put into anhydrous ethanol. Secondly, the temperature was controlled by ultrasound for 1.5 h. Then, the ultrasonic solution was fully stirred in a blender for 36 h. Let the product stand and pour out the supernatant. Finally, the precipitate was put into the oven to dry at 80 °C for 10 h, and the g-C₃N₄/MoS₂-8 composite was collected. The composite materials with mass ratios of 4:1, 6:1, 10:1, 12:1, and 14:1 were prepared according to the above scheme, which were respectively called g-C₃N₄/MoS₂-4, g-C₃N₄/MoS₂-6, g-C₃N₄/MoS₂-10, g-C₃N₄/MoS₂-12, and g-C₃N₄/MoS₂-14.

2.2 Sample characterization

After preparing g-C₃N₄, MoS₂, g-C₃N₄/MoS₂ nanomaterials. X-ray diffractometer (XRD, D/ MAX2400, Rigaku Company, Japan, radiation source Cu K α , tube voltage 40 kV, tube current 30mA), scanning electron microscope (SEM, Hitachi TM3000, Japan), transmission electron microscope (TEM, Fei Talos F200S Super-X spectrometer), X-ray photoelectron spectroscopy (XPS, Thermo Scientific, Escalab XI + type XPS, Al target), UV-Vis spectrometer (UV-Vis, Shimadzu UV3600 Plus) and fluorescence spectroscopy (PL, Yokohama C9920-02G) were used to characterize the composition, morphology and light absorption properties of the materials.

2.3 Photocatalytic tests

The photocatalytic performance of the samples was obtained by the photodegradation pathway of Rh B under visible light irradiation. A 300 W xenon lamp is used to simulate a visible light source. The 50 mg catalyst was dispersed in 50 mL of Rh B solution (the concentration of Rh B was 10 mg/L), and the photocatalyst was stirred with the Rh B solution in the dark for at least 30 min to ensure the adsorption-desorption equilibrium. In the process of photoreaction for 120 min, the concentration of pollutants was analyzed by UV-Vis spectrophotometer after extracting 4 mL of suspension each time and centrifugation. The wavelength range of Rh B was 450–600 nm.

3 Results And Discussion

3.1 XRD analyses

Figure 1 shows the XRD pattern of g-C₃N₄, MoS₂, and g-C₃N₄ /MoS₂-8 complexes. For bulk phase pure g-C₃N₄, MoS₂, and g-C₃N₄ /MoS₂-8 complexes, 35.8° and 58.4° matched the (002), (100),

(102), and (110) crystal faces of hexagonal MoS₂(JCPDS no.37-1492) [28]. Pure g-C₃N₄ and g-C₃N₄/MoS₂-8 complexes have two broadened diffraction peaks at 2θ angles of 13.0° and 27.6°, which are characteristic peaks of g-C₃N₄. They correspond to its (100) and (002) crystal faces [29]. The (002) diffraction peak of the g-C₃N₄/MoS₂-8 composite is weaker than g-C₃N₄. This indicates that MoS₂ does not change the lattice of g-C₃N₄. There is no obvious diffraction peak of MoS₂ in g-C₃N₄ /MoS₂-8, which may be due to the low content of MoS₂.

3.2 SEM and TEM analyses

The microstructure of the g-C₃N₄, MoS₂, and g-C₃N₄/MoS₂-8 were examined by scanning electron microscopy and transmission electron microscopy. Figure 2(a) shows the scanning electron microscope image of the g-C₃N₄. The aggregation structure of unevenly curved nanosheets with some pores, which may be caused by the release of gas during high temperature aggregation. Figure 2(b) shows the SEM figure of the MoS₂, from which it can be seen that the nano-flake MoS₂ is curved and curled up into a spherical shape. Figure 2(c) shows the SEM image of the g-C₃N₄ /MoS₂-8. It can be seen from the figure that the relatively flat g-C₃N₄ nanosheets and the original flower-like MoS₂ nanosheets disappear and become porous and small-area lamellate structures. Particularly, the phenomenon of clustering is obvious. The morphology of the g-C₃N₄/MoS₂ composites was further studied by TEM and HRTEM images. Figure 2(d) shows there are two kinds of nanosheets superposed together. Figure 2(e) shows 0.62nm lattice spacing appears in the composite material, which can be attributed to the (002) crystal plane of MoS₂ [30]. The existence of MoS₂ is also proved. The test of sample element mapping was carried out on the composite material, as shown in Fig. 2(f), and the elements of carbon, nitrogen, molybdenum and sulfur were evenly distributed in the sheet sample. These results show that MoS₂ recombines with g-C₃N₄, indicating the formation of g-C₃N₄ /MoS₂ heterojunction.

3.3 XPS analyses

The chemical compositions and states of carbon, nitrogen, molybdenum, and sulfur in g-C₃N₄/MoS₂-8 heterostructures have been studied by XPS. Figure 3(a) shows that in the C 1s spectrum, there are two peaks at about 284.8 eV and 285.9 eV. The binding energy peak at 284.8 eV corresponds to the C-C group. The peak at 285.9 eV corresponds to the N-C = N group of g-C₃N₄. Figure 3 (b) shows the N 1s spectrum can be fitted to three peaks at 395.3 eV, 397 eV and 401.2 eV, which can be attributed to C-N-C, N-(C)₃ and N-H groups [31]. In the Mo 3d spectrum, three peaks can be observed, which are 224.9 eV, 228.32 eV, and 231.9 eV. It is shown that the Mo element in g-C₃N₄/MoS₂-8 mainly exists in the form of Mo⁴⁺. Figure 3(d) shows the two major peaks at 157.8 eV and 159 eV. The peak of 157.8 eV is attributed to S 2p_{3/2} and 159 eV is attributed to S 2p_{1/2}. They are consistent with S²⁻ in MoS₂. The results show that MoS₂ nanosheets are successfully combined with g-C₃N₄ nanosheets.

Figure 4 shows the UV-Vis diffuse reflectance spectra of the g-C₃N₄ and g-C₃N₄/MoS₂-8 nanosheets. The g-C₃N₄ sample shows the absorption of up to 460 nm in the ultraviolet to visible range, due to the small band gap of g-C₃N₄. To compare with g-C₃N₄, the absorption wavelength of g-C₃N₄/MoS₂-8 composites reaches 475 nm. According to the formula:

$$Eg = 1240 / \lambda g$$

λg is the semiconductor absorption band boundary value, the band gap of g-C₃N₄ is about 2.75 eV. The band gap of g-C₃N₄/MoS₂-8 is about 2.61 eV. The results show that the MoS₂ is successfully combined with g-C₃N₄. The band gap of the photocatalyst decreases with the introduction of MoS₂. Because of the small band gap of MoS₂ and its ability to absorb near-infrared light. Therefore, g-C₃N₄/MoS₂ heterojunction can capture more visible light and enhance the catalytic activity.

3.5 PL analyses

The separation and recombination of photogenerated electron-hole pairs are very important for the performance of catalysts. Figure 5 shows the photoluminescence spectra of the sample. In general, the optical properties of photocatalysts in the visible region can be interpreted as the composition of photogenerated electrons and holes. Figure 5 shows that monomer g-C₃N₄ has a strong fluorescence emission peak at about 450 nm. The results show that in g-C₃N₄ nanomaterials, the electron-hole pair generated by light is easy to combine, which is not good for its photocatalytic performance. The photoluminescence spectra of g-C₃N₄/MoS₂-8 composite photocatalyst decreased obviously. This could inhibit the compound efficiency of photogenerated electrons and holes and improve the activity of photocatalyst.

3.6 Photocatalytic activity analyses

The photocatalytic degradation of g-C₃N₄ and MoS₂ complexes with different mass ratios was studied under visible light irradiation using Rh B as a simulated pollutant. Figure 6 shows the curve of the photocatalytic degradation rate of different photocatalysts over time. The result shows that the g-C₃N₄/MoS₂-8 composite had the best degradation effect. The photodegradation rate of Rh B reached 99.6%. The degradation rate of Rh B by pure g-C₃N₄ was 50% after 120 minutes of light exposure. Therefore, the degradation effect of Rh B by catalyst combined with MoS₂ was nearly 2 times that of pure catalyst.

For low concentrations of organic pollutants, the kinetic behavior of degradation reaction can be studied by the following equation:

$$\ln(C / C_0) = kt$$

C is the concentration of pollutants degraded by photocatalyst ($\text{mg}\cdot\text{L}^{-1}$), C_0 is the adsorption equilibrium concentration of pollutants before radiation ($\text{mg}\cdot\text{L}^{-1}$), t is the reaction time (min), and k is the kinetic constant (min^{-1}). Figure 7 shows the Kinetic constant k of different samples. The k values of $\text{g-C}_3\text{N}_4/\text{MoS}_2$ -8 composites, $\text{g-C}_3\text{N}_4$, and MoS_2 photocatalysts were calculated as 0.0357 min^{-1} , 0.00568 min^{-1} , and 0.00258 min^{-1} . The results show that the degradation rate constant of the composite photocatalyst was 6.3 times of the original $\text{g-C}_3\text{N}_4$ photocatalyst and 13.8 times of the MoS_2 photocatalyst. Therefore, the photocatalytic activity of the composite material for Rh B degradation was significantly improved.

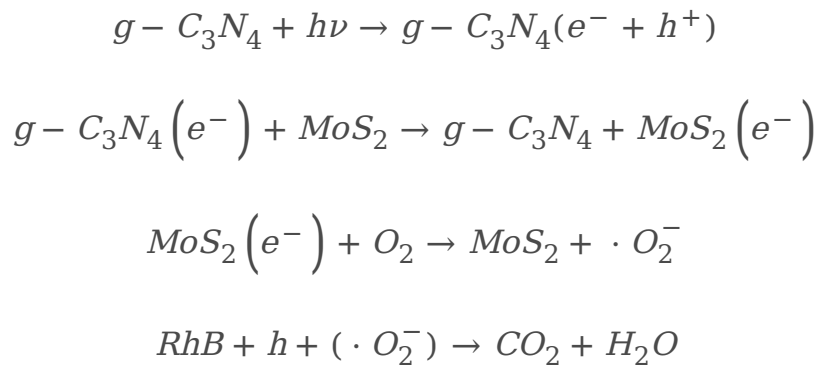
In order to study the photocatalytic stability of $\text{g-C}_3\text{N}_4/\text{MoS}_2$ -8 photocatalyst. The $\text{g-C}_3\text{N}_4/\text{MoS}_2$ -8 powder was cycled five times under the same reaction conditions. Figure 8 shows a relatively stable photocatalytic performance. After five cycles, $\text{g-C}_3\text{N}_4/\text{MoS}_2$ -8 photocatalyst still maintained a relatively high photocatalytic performance for the degradation of Rh B, and the photodegradation rate was 97% after 120 min of illumination. The precipitation and transfer processes may be the main reasons for the degradation of photocatalytic performance. Therefore, $\text{g-C}_3\text{N}_4/\text{MoS}_2$ -8 photocatalyst showed high photocatalytic activity and excellent recoverability for the degradation of organic pollutants under visible light irradiation. This showed great potential for future practical applications.

There are a series of photoinduced active substances such as superoxide radicals ($\cdot\text{O}_2^-$), hydroxyl radicals ($\cdot\text{OH}$) and holes (h^+) in the process of photocatalytic reaction. They will directly participate in the photocatalytic process of Rh B under visible light irradiation. In order to elucidate the role of different substances in the redox reaction, different scavengers were added to the photocatalyst to carry out the reaction. N_2 was added to remove the $\cdot\text{O}_2^-$, isopropanol (IPA) to remove the $\cdot\text{OH}$, and KI to remove the h^+ . The original $\text{g-C}_3\text{N}_4/\text{MoS}_2$ -8 photocatalyst was fed with homogeneous N_2 , 0.5 mmol KI and 0.5 mmol IPA. Their degradation effect on Rh B was measured under visible light irradiation. Figure 9 shows that only 15% of Rh B is degraded by adding KI to the photocatalyst, 93% of Rh B is degraded by adding N_2 to the photocatalyst, and 97% of Rh B is degraded by adding isopropanol. It can be seen that all three substances participate in the photocatalytic reaction. But the main role is the h^+ followed by the $\cdot\text{O}_2^-$.

Figure 10 illustrates the mechanism of improving the photocatalytic activity of the $\text{g-C}_3\text{N}_4/\text{MoS}_2$ composite. Under illumination, $\text{g-C}_3\text{N}_4$ absorbs visible light and is excited to produce photogenerated electron-hole pairs. The photogenerated electrons transition from the valence band (VB) to the conduction band (CB) and leave holes in the valence band. According to the theoretical values, the conduction band potentials (E_{CB}) of $\text{g-C}_3\text{N}_4$ is about -1.22 eV and MoS_2 is about -0.12 eV . The band gaps between them are about 2.88 eV and 1.90 eV . Then according to:

$$E_{\text{VB}} = E_{\text{CB}} + E_g$$

it can be seen that their valence band potentials (E_{VB}) are about 1.66 and 1.78 eV [32]. They have a matching band structure. When g-C₃N₄ and MoS₂ are combined. Since the CB potential of g-C₃N₄ is more negative than MoS₂. The photoinduced electrons in the CB of g-C₃N₄ can be easily transferred to the CB of MoS₂ through the interface. At the same time, because the VB position of g-C₃N₄ is more negative than MoS₂. The holes in the VB of MoS₂ move to the VB position of g-C₃N₄ in a similar manner, facilitating the separation of the photogenerated electrons from the holes. Electrons are collected in CB of MoS₂ and the holes are collected in VB of g-C₃N₄. Therefore, the probability of electron-hole recombination is hindered. It can reduce the probability of photo-generated carrier recombination and prolongs the life of the photo-generated carrier. Therefore, the photocatalytic activity is improved. According to the report, the redox potential of OH⁻ / •OH is about 2.27 eV [33]. Therefore, the holes generated in the VB cannot directly oxidize the OH⁻ or water molecules adsorbed on the surface of the catalyst to •OH directly. But directly oxidize the organic matter in the form of holes. So one of the main active species in the photocatalytic experiment is the hole. On the other hand, the photogenerated electrons transferred to MoS₂ have higher reducing power. The redox potential of O₂/•O₂⁻ is about 0.33 eV [34]. It can react with O₂ adsorbed on the catalyst surface to generate •O₂⁻. So the other major reactive agent is the •O₂⁻. And get the following equation:



Therefore, through the above analysis, it can be expected that the photodegradation activity of the photocatalyst can be effectively improved by forming the g-C₃N₄/MoS₂ heterojunction.

4 Conclusion

The g-C₃N₄ nanosheets and MoS₂ nanosheets were synthesized by thermal polymerization and hydrothermal method. Then ultrasonically composited with g-C₃N₄. The g-C₃N₄/MoS₂ composite material was obtained simply. The experiment of photocatalytic degradation of Rh B shows that under the irradiation of visible light, the composite of a small amount of MoS₂ significantly improves the photocatalytic activity of g-C₃N₄. The best photocatalytic activity was that the g-C₃N₄/MoS₂ composite with a mass ratio of 8:1. The degradation effect can reach 99.6% after 120 min of illumination. The active matter capture experiment shows that the main active matter in the photocatalytic reaction process is holes, followed by superoxide radicals. UV-Vis diffuse reflectance shows that the band gap of

g-C₃N₄/MoS₂ composite also shows good light stability. The above results show that the material has good application prospects in the photocatalytic treatment of organic pollutants.

Declarations

Acknowledgments

This study was funded by the National Natural Science Foundation of China (61664008), Yan 'an Science and Technology Planning Project (2019ZCNZ-001); Yan 'an University Industry-University-Research Cooperation Project (CXY201902); Research Fund for key Laboratories jointly built by provinces and cities of Shaanxi Province for Intelligent Processing of Big Data (IPBED11, IPBED16); Graduate Education Reform Program of Yan 'an University (YDYJG2019018).

References

1. S. Palanivel, A. Mani, P. Thayumanavan, Utilization of agro-industrial waste *Jatropha curcas* pods as an activated carbon for the adsorption of reactive dye Remazol Brilliant Blue R (RBBR). *J Clean Prod* **22**(1), 67–75 (2012)
2. N. Li, H. Gao, X. Wang, S.J. Zhao, D. Lv, G.Q. Yang, X.Y. Gao, H.K. Fan, Y.Q. Gao, L. Ge, Novel indirect Z-scheme g-C₃N₄/Bi₂MoO₆/Bi hollow microsphere heterojunctions with SPR-promoted visible absorption and highly enhanced photocatalytic performance. *Chinese J Cataly* **41**(03), 426–434 (2020)
3. B.X. Zhang, S.X. Cao, M.Q. Du, X.Z. Ye, Y. Wang, J.F. Ye, Titanium Dioxide (TiO₂) Mesocrystals: Synthesis, Growth Mechanisms and Photocatalytic Properties. *Catalysts* **9**(1) (2019)
4. H. Park, Y. Park, W. Kim, W. Choi, Surface modification of TiO₂ photocatalyst for environmental applications (Review). *J Photoch Photobio C* **15**(1), 1–20 (2013)
5. B.A. Carlos, J.G. Javier, A. Raul, L. Marta, B.P. Bruno, H. Jose, L., Anisotropic Au-ZnO photocatalyst for the visible-light expanded oxidation of n-hexane. *Cataly Today* **362**, 97–103 (2021)
6. J.A. Quek, J.C. Sin, S.M. Lam, A.R. Mohamed, H.H. Zeng, Bioinspired green synthesis of ZnO structures with enhanced visible light photocatalytic activity. *J Mater Sci-Mater El* **31**(2), 1144–1158 (2020)
7. S.Q. Wu, H.Y. Hu, Y. Lin, J.L. Zhang, Y.H. Hu, Visible light photocatalytic degradation of tetracycline over TiO₂. *Chem. Eng. J.* **382**, 122842 (2020)
8. Y.P. Xie, Z.B. Yu, G. Liu, X.L. Ma, H.M. Cheng, Cds-mesoporous ZnS core-shell particles for efficient and stable photocatalytic hydrogen evolution under visible light. *Energ Environ Sci* **7**(6), 1895–1901 (2014)
9. J.H. Liu, G.F. Huang, W.Q. Huang, H. Miao, B.X. Zhou, Morphology-controlled SnS₂ nanostructures synthesized by refluxing method with high photocatalytic activity. *Mater Lett* **161**(1), 480–483 (2015)

10. A.D. Di, Y. Wang, G. Chen, Dendritic hierarchical AgCl prepared in the interface of gas-solid as the precursors of the visible-light plasmonic photocatalysts of Ag–AgCl. *Funct Mater Lett* **11**(1), 1850006 (2018)
11. Y.Q. Yang, R.X. Liu, G.K. Zhang, L.Z. Gao, W.K. Zhang, Preparation and photocatalytic properties of visible light driven Ag–AgCl–TiO₂/palygorskite composite. *J. Alloy. Compd.* **657**, 801–808 (2016)
12. W.K. Ji, Z.B. Rui, H.B. Ji, Z-scheme Ag₃PO₄/Ag/SrTiO₃ Heterojunction for Visible-Light Induced Photothermal Synergistic VOCs Degradation with Enhanced Performance. *Ind. Eng. Chem. Res.* **58**(31), 13950–13959 (2019)
13. A. Tab, B. Bellal, C. Belabed, M. Dahmane, M. Trari, Visible light assisted photocatalytic degradation and mineralization of Rhodamine B in aqueous solution by Ag₃PO₄. *Optik* **214**, 164858 (2020)
14. X.Y. Gao, W. Peng, G.B. Tang, Q. Guo, Y.M. Luo, Highly efficient and visible-light-driven BiOCl for photocatalytic degradation of carbamazepine. *J. Alloy. Compd.* **757**, 455–465 (2018)
15. Z.L. Liu, F.Y. Lv, Y. Xiao, B. Chen, J. Qiu, W.Z. Guo, Y. Wen, Z. Li, Z.S. Liu, Mor-phologycontrollable synthesis of BiOBr architectures and their visible light photocatalytic activities. *Mater. Technol.* **34**(11), 683–688 (2019)
16. X.C. Wang, K. Maeda, A. Thomas, K. Takanabe, G. Xin, J.M. Carlsson, K. Domen, M. Antonietti, A metal-free polymeric photocatalyst for hydrogen production from water under visible light. *Nat. Mater.* **8**(1), 76–80 (2009)
17. J. Li, E.Z. Liu, Y.N. Ma, X.Y. Hu, J. Wan, L. Sun, J. Fan, Synthesis of MoS₂/g-C₃N₄ nanosheets as 2D heterojunction photocatalysts with enhanced visible light activity. *Appl Surf Sci* **364**, 694–702 (2016)
18. M. Zhang, X.J. Bai, D. Liu, J. Wang, Y.F. Zhu, Enhanced catalytic activity of potassium-doped graphitic carbon nitride induced by lower valence position. *Appl. Catal. B* **164**, 77–81 (2015)
19. D.D. Xu, X.N. Li, J. Liu, L.H. Huang, Synthesis and photocatalytic performance of europium-doped graphitic carbon nitride. *J. Rare Earths* **31**(11), 1085–1091 (2013)
20. N.Y. Cheng, J.Q. Tian, Q. Liu, C.J. Ge, A.H. Qusti, A.M. Asiri, A.O. Al-Youbi, X.P. Sun, Au-nanoparticle-loaded graphitic carbon nitride nanosheets: green photocatalytic synthesis and application toward the degradation of organic pollutants. *ACS Appl Mater Inter* **5**(15), 6815–6819 (2013)
21. Y.L. Meng, J. Shen, D. Chen, G. Xin, Photodegradation performance of methylene blue aqueous solution on Ag/g-C₃N₄ catalyst. *Rare Met.* **30**(s1), 276–279 (2011)
22. Y.G. Wang, Y.Z. Wang, Y.T. Chen, C.C. Yin, Y.H. Zuo, L.F. Cui, Synthesis of Ti-doped graphitic carbon nitride with improved photocatalytic activity under visible light. *Mater Lett* **139**, 70–72 (2015)
23. J.L. Chen, Z.H. Hong, Y.L. Chen, B.Z. Lin, B.F. Gao, One-step synthesis of sulfur-doped and nitrogen-deficient g-C₃N₄ photocatalyst for enhanced hydrogen evolution under visible light. *Mater Lett* **145**, 129–132 (2015)
24. M.L. Li, L.X. Zhang, X.Q. Fan, M.Y. Wu, Y.Y. Du, M. Wang, Q.L. Kong, L.L. Zhan-g, J.L. Shi, Dual synergistic effects in MoS₂/graphitic carbon nitride composite for highly active and stable

- photocatalytic hydrogen evolution under visible light. *Appl Catal B* **190**, 36–43 (2016)
25. X. Yan, Q. Gao, X. Hui, C. Yan, T. Ai, Z. Wang, G. Sun, X. Su, P. Zhao, Fabrication of g-C₃N₄/MoS₂ Nanosheet Heterojunction by Facile Ball Milling Method and Its Visible Light Photocatalytic Performance. *Rare Metal Mat Eng* **47**(10), 3015–3020 (2018)
 26. L. Ge, C.C. Han, X.L. Xiao, L.L. Guo, Synthesis and characterization of composite visible light active photocatalysts MoS₂-C₃N₄ with enhanced hydrogen evolution activity. *Int J Hydrog Energy* **38**(17), 6960–6969 (2013)
 27. Q. Li, N. Zhang, Y. Yang, G.Z. Wang, N.H.L. Dickon, High Efficiency photocatalysis for pollutant degradation with MoS₂/C₃N₄ heterostructures. *Langmuir* **30**(29), 8965–8972 (2014)
 28. W.J. Zhou, Z.Y. Yin, Y.P. Du, X. Huang, Z.Y. Zeng, Z.X. Fan, H. Liu, J.Y. Wang, H. Zhang, Synthesis of few-layer MoS₂ nanosheet-coated TiO₂ nanobelt heterostructures for enhanced photocatalytic activities. *Small* **9**(1), 140–147 (2013)
 29. Y.N. Ma, E.Z. Liu, X.Y. Hu, C.N. Tang, J. Wan, J. Li, J. Fan, A simple process to prepare few-layer g-C₃N₄ nanosheets with enhanced photocatalytic activities. *Appl Surf Sci* **358**(Part A), 246–251 (2015)
 30. L. Guo, Z. Yang, K. Marcus, Z. Li, B. Luo, L. Zhou, X. Wang, Y. Du, Y. Yang, MoS₂/TiO₂ heterostructures as nonmetal plasmonic photocatalysts for highly efficient hydrogen evolution. *Energy Environ Sci* **11**(1), 106–114 (2017)
 31. X.F. Yang, Z.P. Chen, J.S. Xu, H. Tang, K.M. Chen, Y. Jiang, Tuning the morphology of g-C₃N₄ for improvement of Z-scheme photocatalytic water oxidation. *ACS Appl Mater Inter* **7**(28), 15285–15293 (2015)
 32. M.J. Lucero, J.K. Ellis, G.E. Scuseria, The indirect to direct band gap transition in multilayered MoS₂ as predicted by screened hybrid density functional theory. *Appl phys lett* **99**(26), 261908 (2011)
 33. X. Chen, P.F. Tan, B.H. Zhou, H.G. Dong, J. Pan, X. Xiong, A green and facile strategy for preparation of novel and stable Cr-doped SrTiO₃/g-C₃N₄ hybrid nanocomposites with enhanced visible light photocatalytic activity. *J. Alloys Compd.* **647**(15), 456–462 (2015)
 34. H.L. Lv, G.B. Ji, Z.H. Yang, Y.S. Liu, X.M. Zhang, W. Liu, H.Q. Zhang, Enhancement photocatalytic activity of the graphite-like C₃N₄ coated hollow pencil-like ZnO. *J. Colloid Interface Sci.* **450**, 381–387 (2015)

Figures

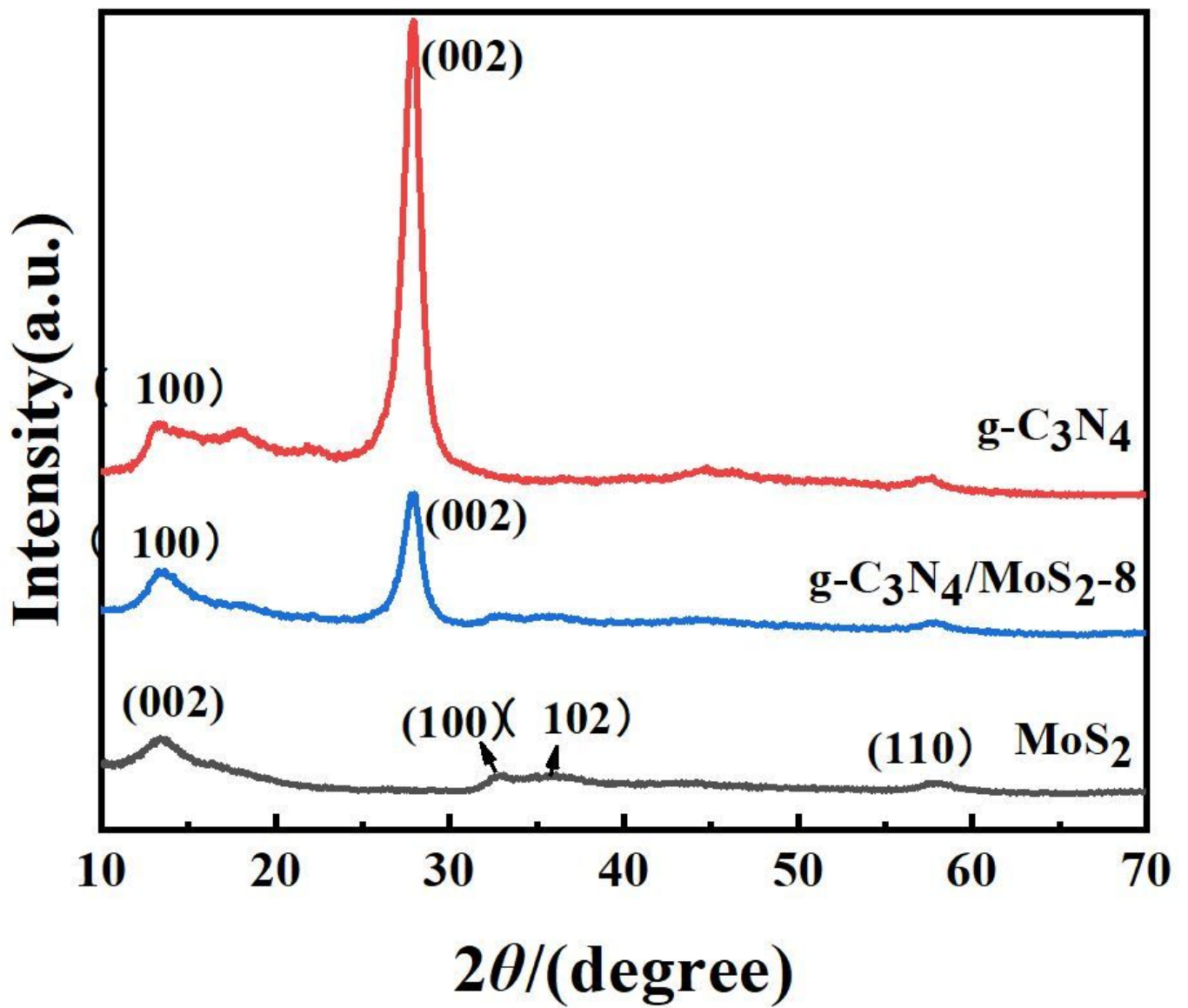


Figure 1

XRD patterns of g-C₃N₄, g-C₃N₄/MoS₂ composite, and MoS₂

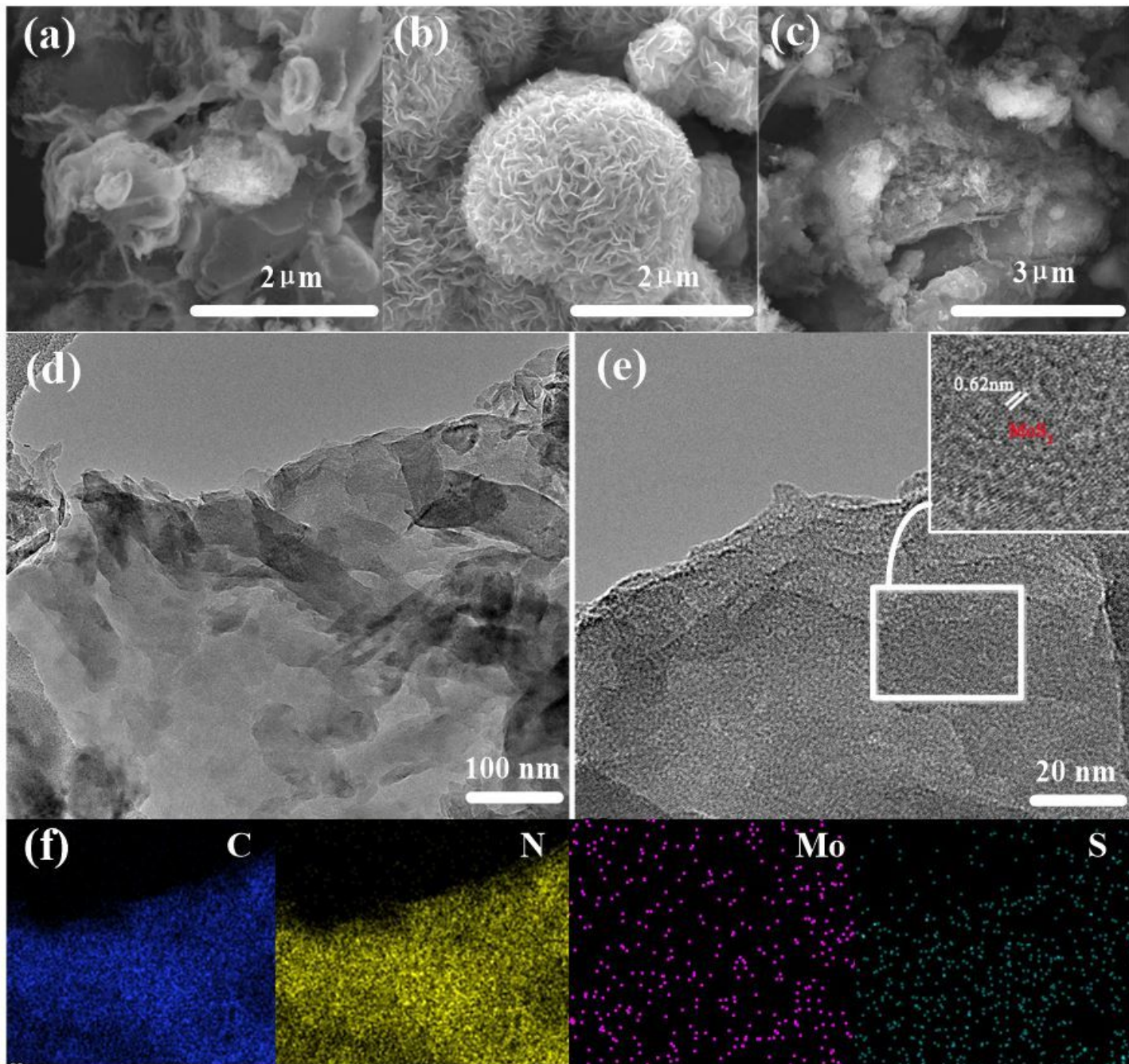


Figure 2

SEM diagram of g-C₃N₄ (a), MoS₂ (b), g-C₃N₄ /MoS₂ (c) composite; TEM images of g-C₃N₄ /MoS₂-8 composite (d); HRTEM images of g-C₃N₄ /MoS₂-8 composite (e); g-C₃N₄ /MoS₂-8 complex element mapping (f), C element, N element, Mo element, S element

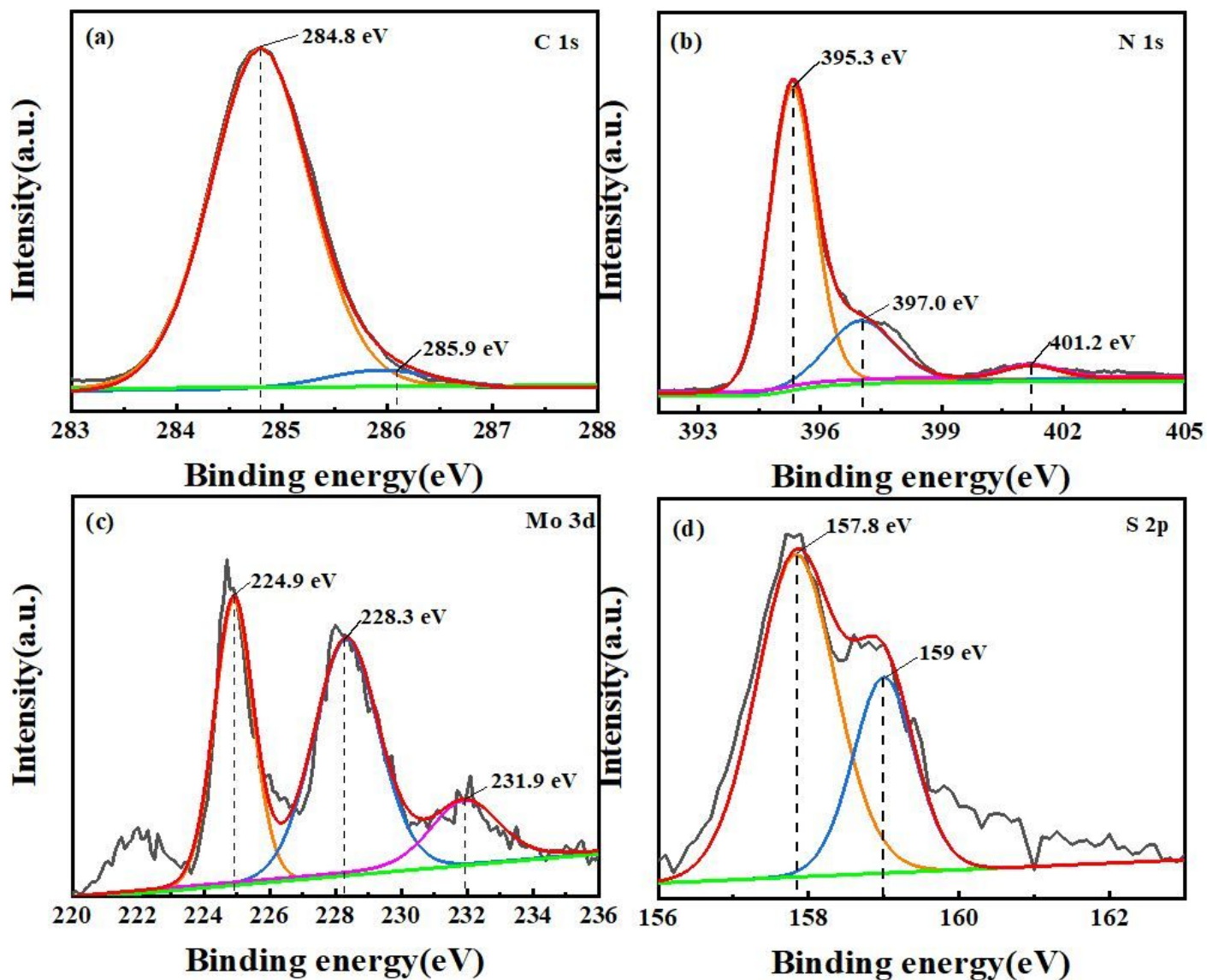


Figure 3

XPS spectra of g-C₃N₄/MoS₂-8

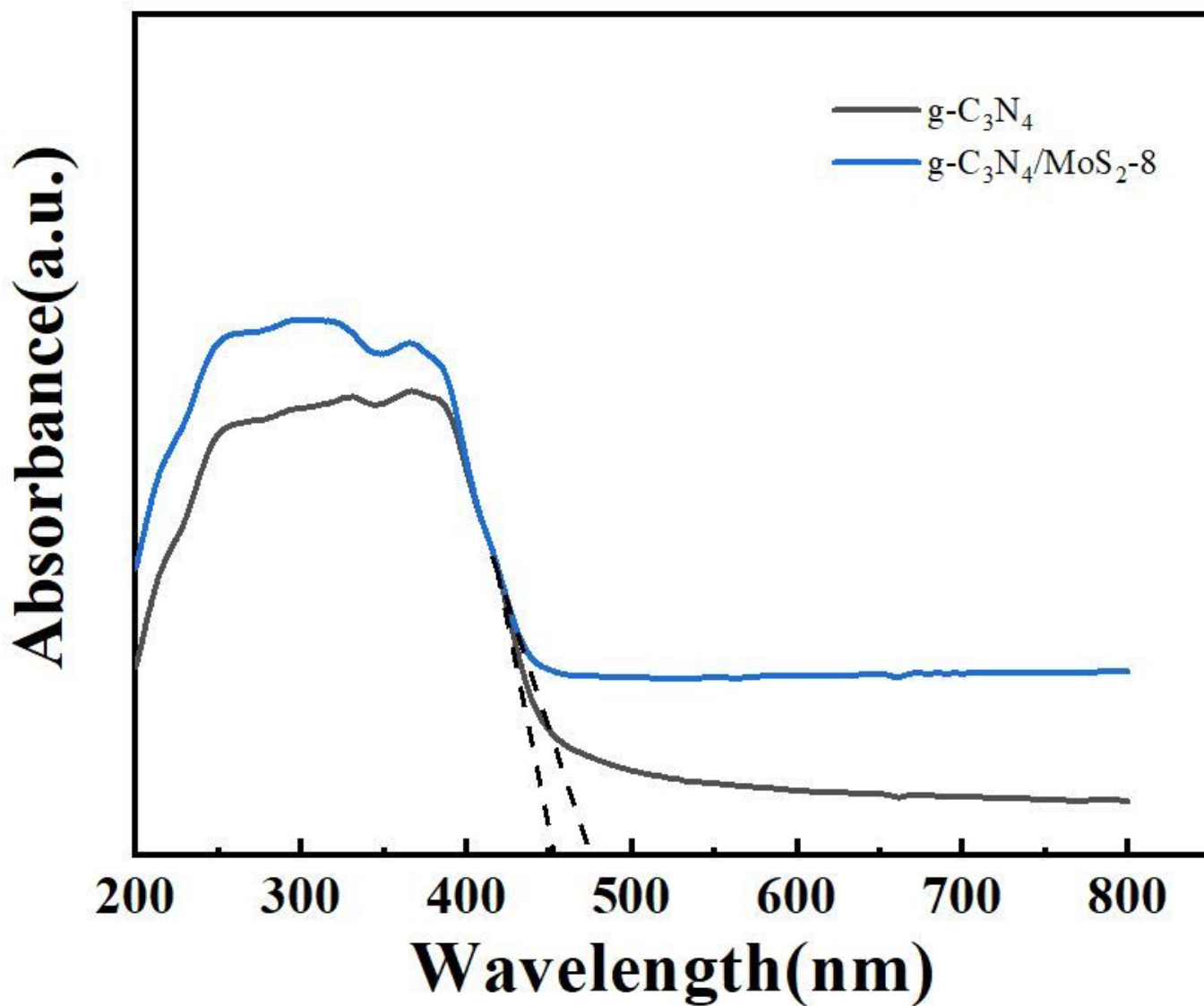


Figure 4

UV-Vis spectra of g-C₃N₄, MoS₂, and g-C₃N₄/MoS₂-8 composite

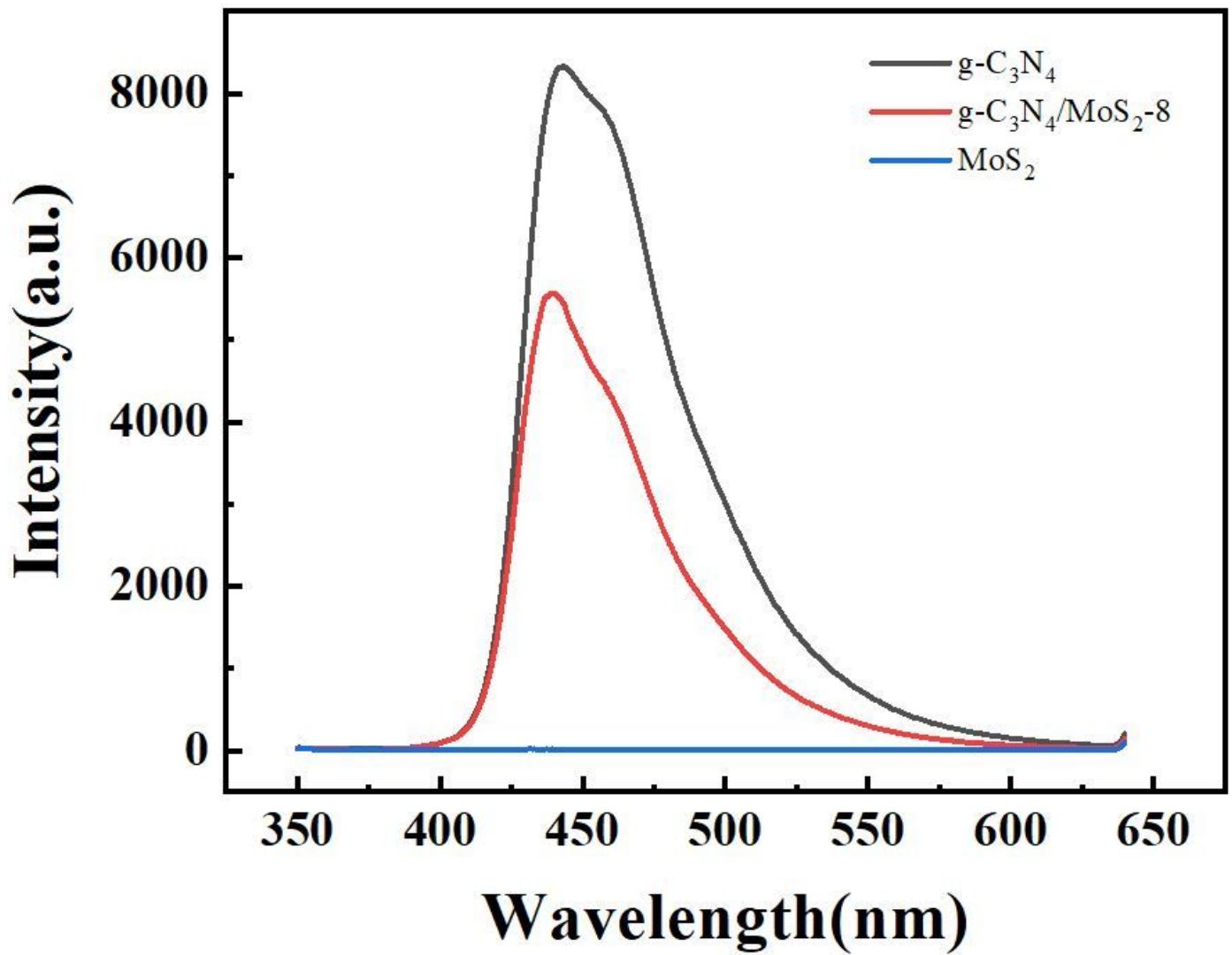


Figure 5

PL spectra of g-C₃N₄, MoS₂, and g-C₃N₄/MoS₂-8 composite

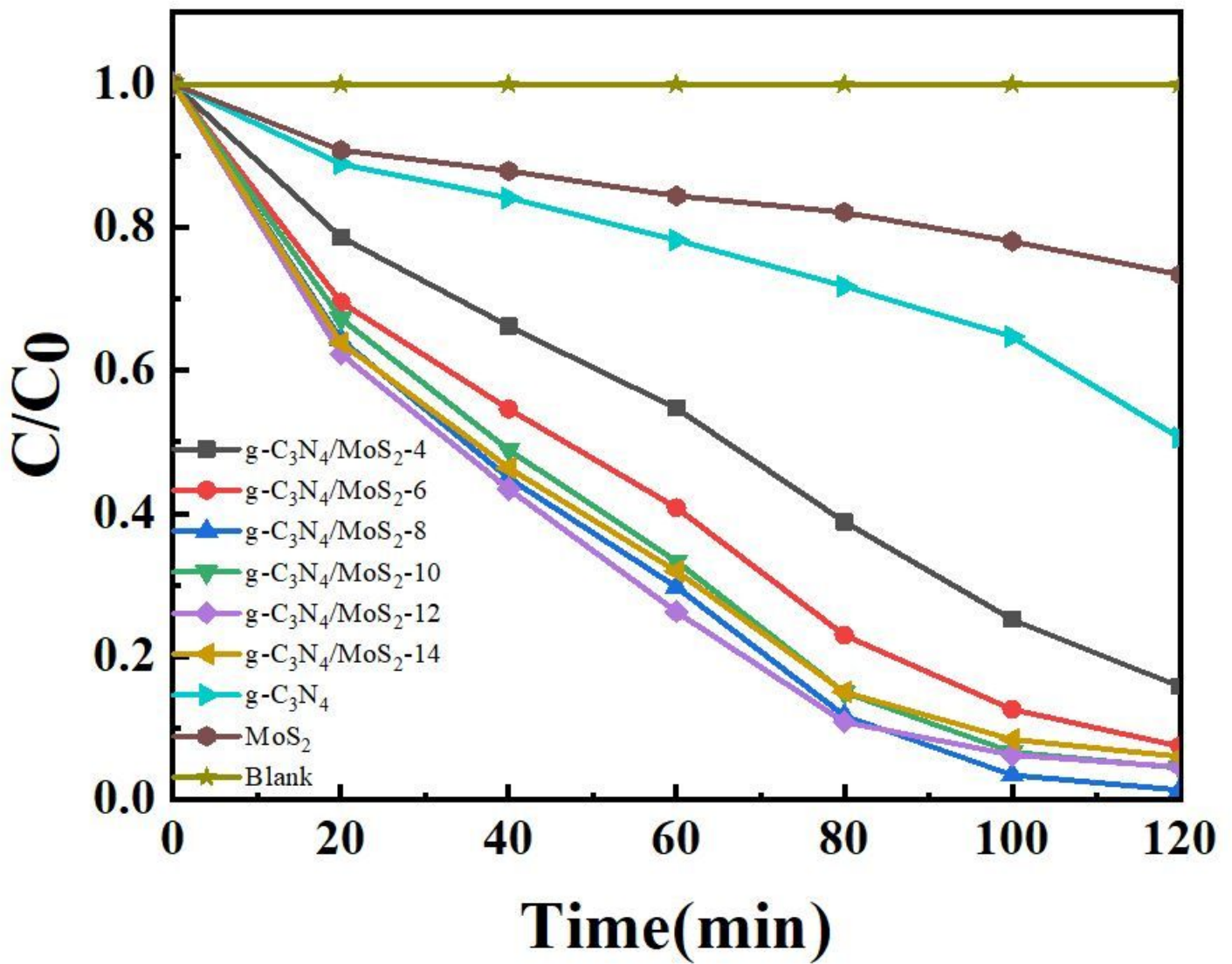


Figure 6

Photocatalytic degradation curve of Rh B solution by different samples

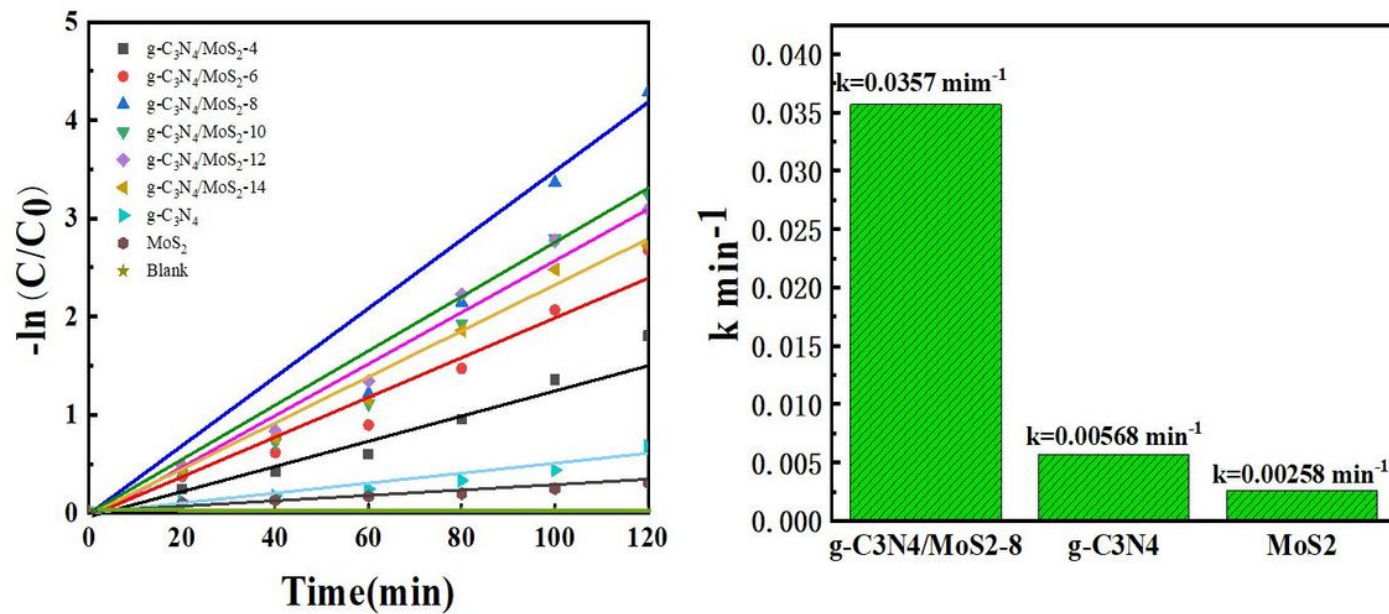


Figure 7

Photocatalytic reaction rate constants of different samples

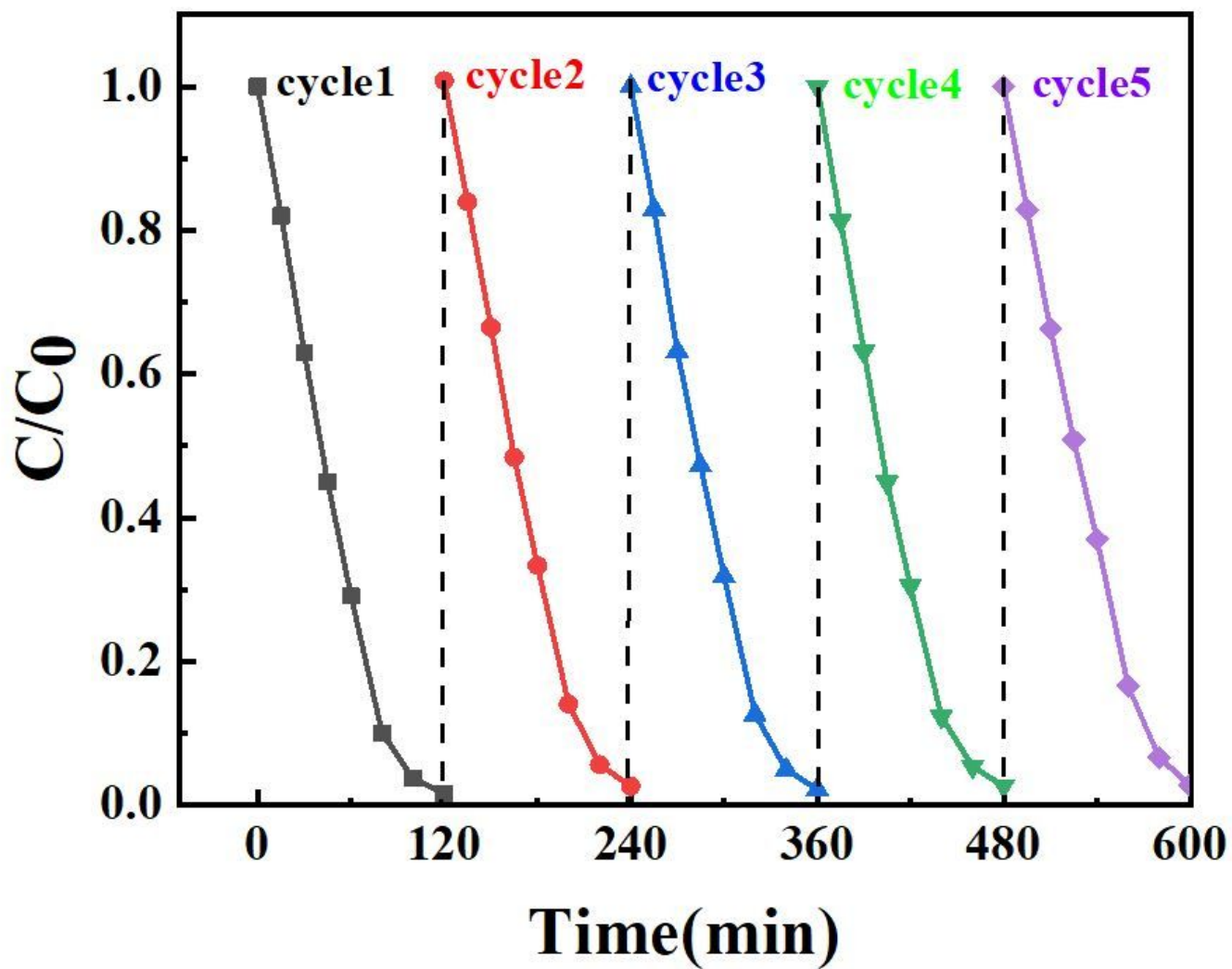


Figure 8

Cyclic degradation curve of g-C3N4/MoS2-8 composite

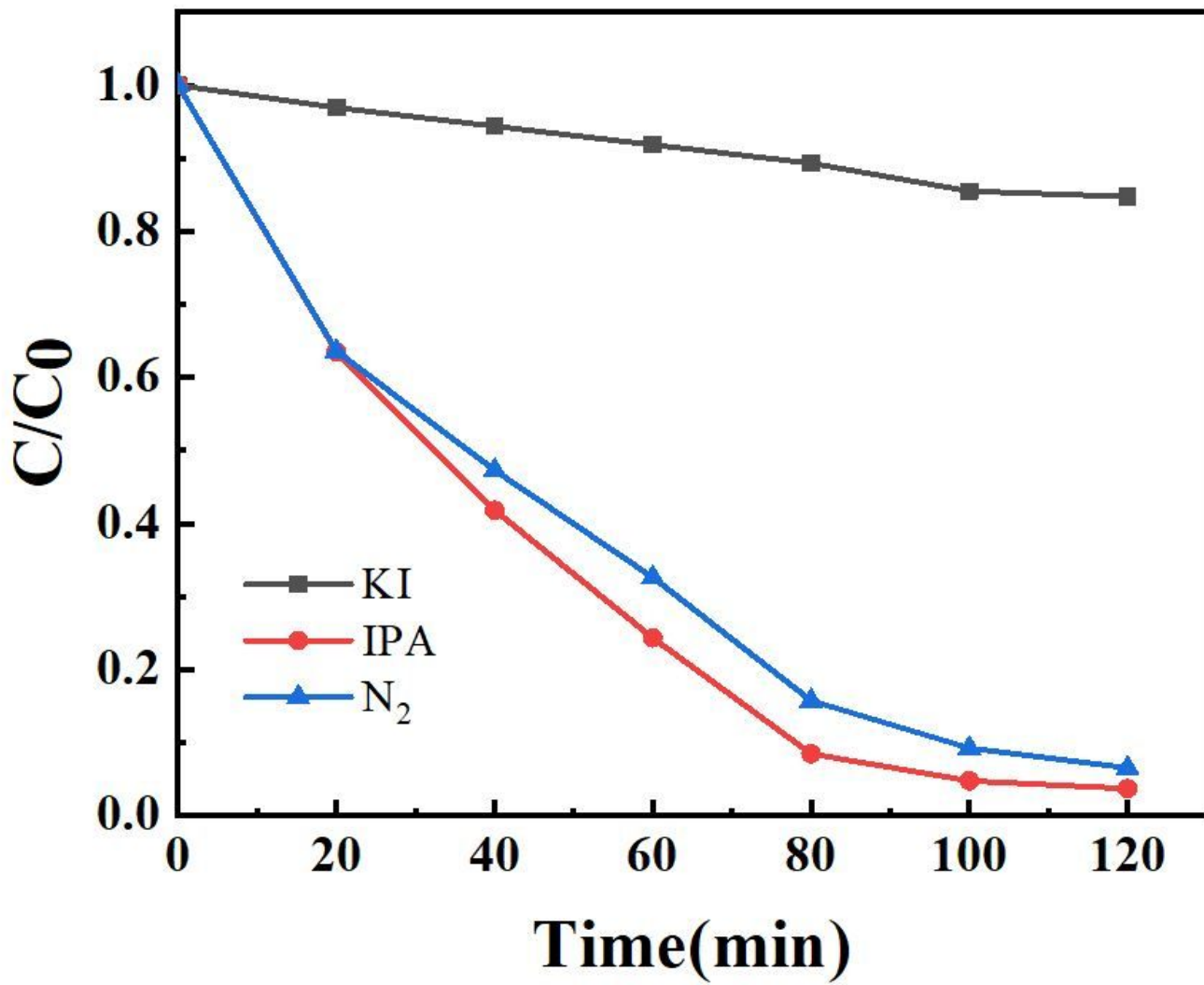


Figure 9

The effect of the trapping agent on the photocatalytic activity

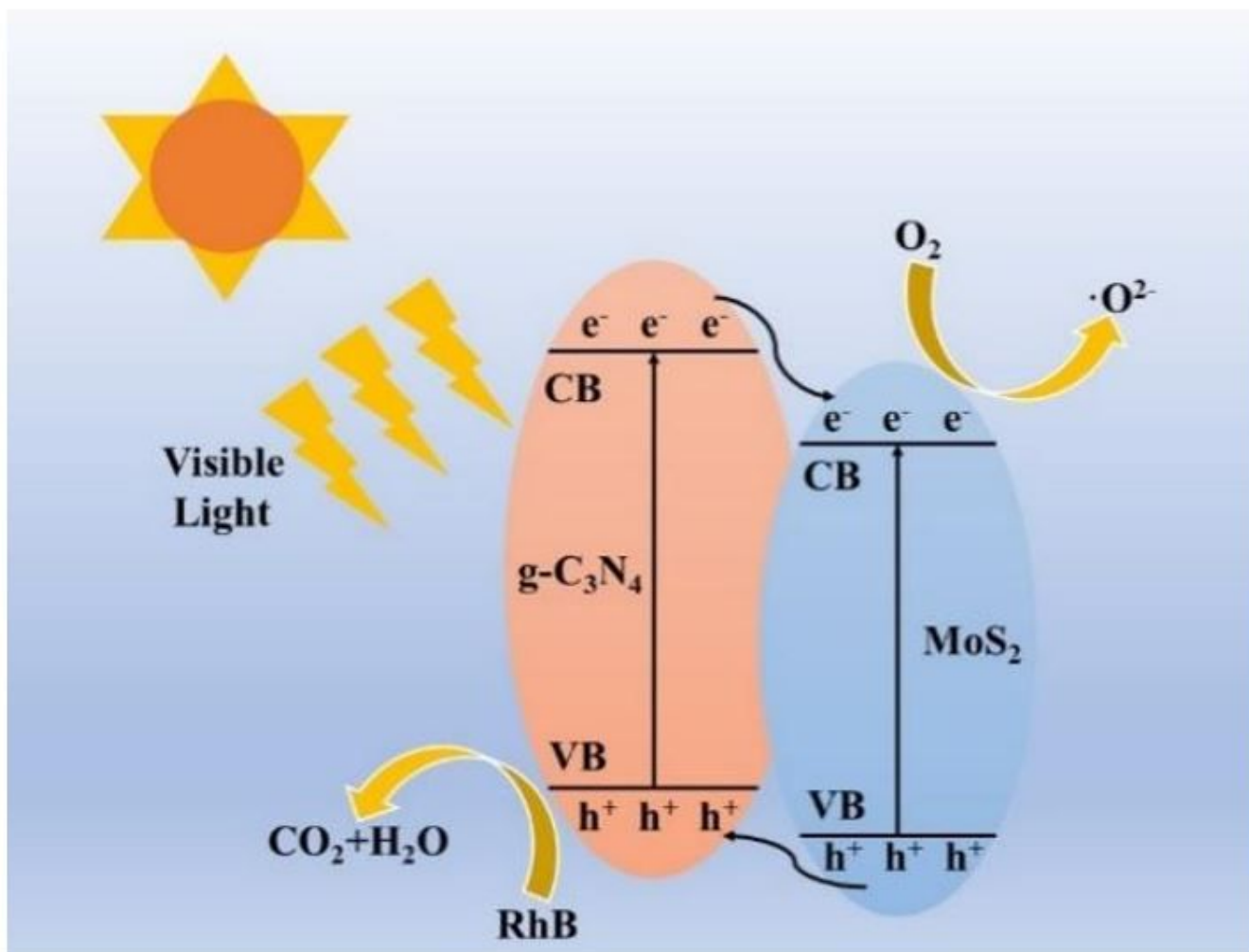


Figure 10

Photocatalytic enhancement mechanism diagram of g-C₃N₄/MoS₂-8 composite